Original research article

I·M3
Institute of Materials, Minerals & Mining

Tribology - Materials, Surfaces & Interfaces
1–11

DOI: 10.1177/17515831261422305
journals.sagepub.com/home/trb


Low friction glaze layer formation during lubricated dynamic pressure sliding of grade 250 flake graphite cast iron

John Walker[1], Timothy Kamps[2] and Keith Paton[2]

Abstract

Evaluating scuffing resistance of new materials for reciprocating engine components can be achieved using dynamic pressure sliding. Surface species responsible for low friction behaviour observed prior to scuffing initiation in a Grade 250 flake graphite cast iron under dynamic pressure (8–62 MPa) sliding conditions experienced by a heavy-duty diesel engine top compression ring were evaluated. Lubricated reciprocating tribometer tests were performed in a polyalphaolefin base oil with temperature incremented to 250 °C to induce scuffing. Friction and contact potential measurements revealed a transition from mixed to boundary lubrication, followed by a period of low friction preceding scuffing initiation. Post-test surface analysis was conducted using a range of advanced microscopy techniques (Raman, FIB, STEM, EDX and EELS) and suggested a complex series of tribochemical reactions are responsible for formation and removal of phases such as siloxanes and ferrous oxides that lead to the initiation of scuffing.

Keywords

scuffing, 'glaze' layer, oxidative wear, cast iron, friction

Received: 10 October 2025; accepted: 23 January 2026

Introduction

Transitioning to green sources of energy in the transport sector entails the use of new and innovative fuel sources such as hydrogen, ammonia, methanol[1–5] or fuels derived through gasification of waste streams.[6] The influence of such fuels on existing engine materials is less clear, particularly for tribological components which involve relative motion between surfaces.[7] Fuel chemistry and engine operating temperature can facilitate the presence of species capable of lubricant degradation (e.g., condensed water vapour,[8] steam from hydrogen combustion[9]) or surface corrosion (e.g., ammonia[10]).

Screening new materials for scuffing resistance in sustainably fuelled engines can be expensive given the multiplicity of factors involved in their operation. Whilst laboratory bench testing offer an intermediate compromise between fundamental materials science and the demands of an engineering application, they often used over a narrow set of operating parameters.[10–12] This can necessitate either complex test protocols which may mask transitory surface evolution or else multiple tests at constant conditions, increasing the duration and cost of the test campaign.

There have been numerous attempts to improve the accuracy of benchtop tribometer sliding contact conditions,[13] including the use of profiled cam/follower arrangements for application of normal loads.[14,15] More recently, dynamic pressure sliding has been shown as an effective approach to better represent contact pressures experienced by a sliding engineering component in a bench-top laboratory tribometer.[16–18] Application of this technique to investigate scuffing behaviour in Grade 250 flake graphite cast iron materials used for heavy duty diesel cylinder liners has shown that the presence of surface tribofilms play an important role in the evolution of the tribological contact prior to the onset of scuffing. Specifically, the formation of oxide layers has a precursive role in the transition of lubricated sliding contacts into scuffing initiation.[19–24] These layers sometimes facilitate transitions to lower friction prior to scuffing,[22,25] however the exact mechanism as to why some contact exhibit this behaviour and others do not remains elusive.[16,17]

This paper investigates the surface chemistry of a dynamic pressure sliding Grade 250 flake graphite cast iron after it has been subject to elevated temperature

[1]National Centre for Advanced Tribology (nCATS), University of Southampton, Southampton, UK
[2]National Physical Laboratory, Teddington, UK

Corresponding author:
John Walker, National Centre for Advanced Tribology (nCATS), University of Southampton, Southampton, UK.
Email: j.walker@soton.ac.uk

scuffing up to 250°C. A range of surface analytical techniques including Raman spectroscopy, focused ion beam (FIB), scanning transmission electron microscopy (STEM) combined with energy dispersive X-ray spectroscopy (EDX) and electron energy loss spectroscopy (EELS) were used to elucidate the nature of the surface species that give rise to the low friction behaviour observed prior to the onset of scuffing. Combining the use of dynamic pressure sliding with these advanced characterisation techniques allows a novel understanding of the complex surface chemistry evolution that governs the observed friction behaviour prior to scuffing.

Methodology

Specimen preparation

A billet of Grade 250 flake graphite cast iron with nominal composition detailed in Table 1 was procured from West Yorkshire Steel Ltd, UK and sectioned into plates of dimensions $58 \times 38 \times 3.8$ mm. Standard metallographic procedures were used to polish a sample to 1 μm diamond followed by a colloidal silica finish, producing an average surface roughness R_a of 0.025 ± 0.005 μm. The microstructure was imaged using an Olympus optical microscope. A dynamic pressure profile of a top compression ring in a heavy duty 12.8 litre naturally aspirated diesel engine was manufactured according to the methodology outlined in Walker et al.[17] using an end mill to introduce a 1 mm recess, Figure 1(a)). This design facilitated a change in contact pressure when a normal load of 311 N was applied through a bainitic 52100 rectangular reciprocating counter surface of dimensions 1.97×20.00 mm, surface roughness (R_a) of 2.12 ± 0.14 μm[17] and Vickers microhardness of 776 ± 52 for a 500 gf load. When the entire rectangular surface was in contact, a nominal pressure of 7.9 MPa would be exerted, whereas when the same rectangular surface transitioned the narrow constriction, the nominal contact pressure would rise to a peak of 61.7 MPa. The surface of the cast iron coupon was ground at 45 ° to the sample edges in order to simulate a honed surface, with an average surface roughness, R_a, of 1.04 ± 0.09 μm.

Dynamic pressure sliding

Lubricated reciprocating sliding was conducted using Phoenix Tribology TE77 High Frequency Reciprocating Tribometer, shown schematically in Figure 1(b)). The dynamic pressure cast iron coupon and rectangular 52100 counter surface were immersed in a bath of polyalfaolefin (Spectrasyn 4) of 4 cSt viscosity at 100°C. Reciprocating sliding was conducted at 15 Hz frequency over a stroke length of 25 mm. An initial normal load of 5 N was applied over a period of 20 s whilst the counter surface accelerated to the test frequency. The load was then ramped up to the test load of 311 N over a period of 300 s. Once the test load had been achieved, an open loop temperature ramp to 250°C commenced at a rate of 4°C/min. Stroke resolved friction force (10 N/V) and contact potential (0–55 mV) signals were recorded at an acquisition rate of 15 kHz through the test. The friction force transducer amplifier outputs an alternating waveform corresponding to the reciprocating force vector arising from the sliding interface. This waveform is rectified and averaged over 1.4 s using a true Root Mean Square (RMS) to DC converter which is sampled every second and reported as the average friction force. This is the default operating mode of this commercially available tribometer and enables average friction coefficient values to be calculated by dividing by the recorded normal load. The onset of scuffing was detected by a rapid rise in the average coefficient of friction.[20,22,25] Three tests were conducted to ensure the repeatability of the results as detailed in Walker *et al.*[17]

Table 1. Nominal wt% composition of Grade 250 cast iron.

Carbon	Silicon	Phosphorous	Manganese	Sulphur	Iron
2.90–3.65	1.80–2.90	< 0.3	0.40–0.70	<0.1	Balance

Raman

Raman spectroscopy was carried out using a Renishaw InVia confocal spectrometer (Renishaw Ltd, UK). A 532 nm excitation laser (~1 mW at the sample) was used to acquire spectra, with 10 s acquisition time and a 100× magnification objective lens (NA = 0.9). Mapping was carried out over an area 28×28 μm, with 2 μm steps. A polynomial baseline was fitted and subtracted from the spectra and a non-negative least squares fitting applied. Reference spectra for hematite and magnetite were taken from the Renishaw Library.

Focused ion beam

A Carl Zeiss NVison 40 combined focused ion beam (FIB) and Scanning Electron Microscope (SEM) was used to manufacture a transmission electron microscopy (TEM) specimen from the sub-surface region within the high pressure contact zone. An initial deposition of Pt over the area of interest was used to protect the top surface using the electron beam, followed by ion beam deposition of carbon. The lamella was ion milled and extracted to a copper TEM grid using an in-situ manipulator (Kliendiek) prior to final thinning to electron transparency. The sample was then plasma cleaned to reduce the risk of contamination during TEM analysis.

Scanning transmission electron microscopy

A JEOL ARM200F aberration corrected scanning transmission electron microscope was used to image the extracted lamella at 200 keV using a combination of bright and annual dark field images. A JEOL 100 mm^2 X-ray detector was used for the acquisition of both line scans and elemental maps. Electron energy loss spectroscopy (EELS) was

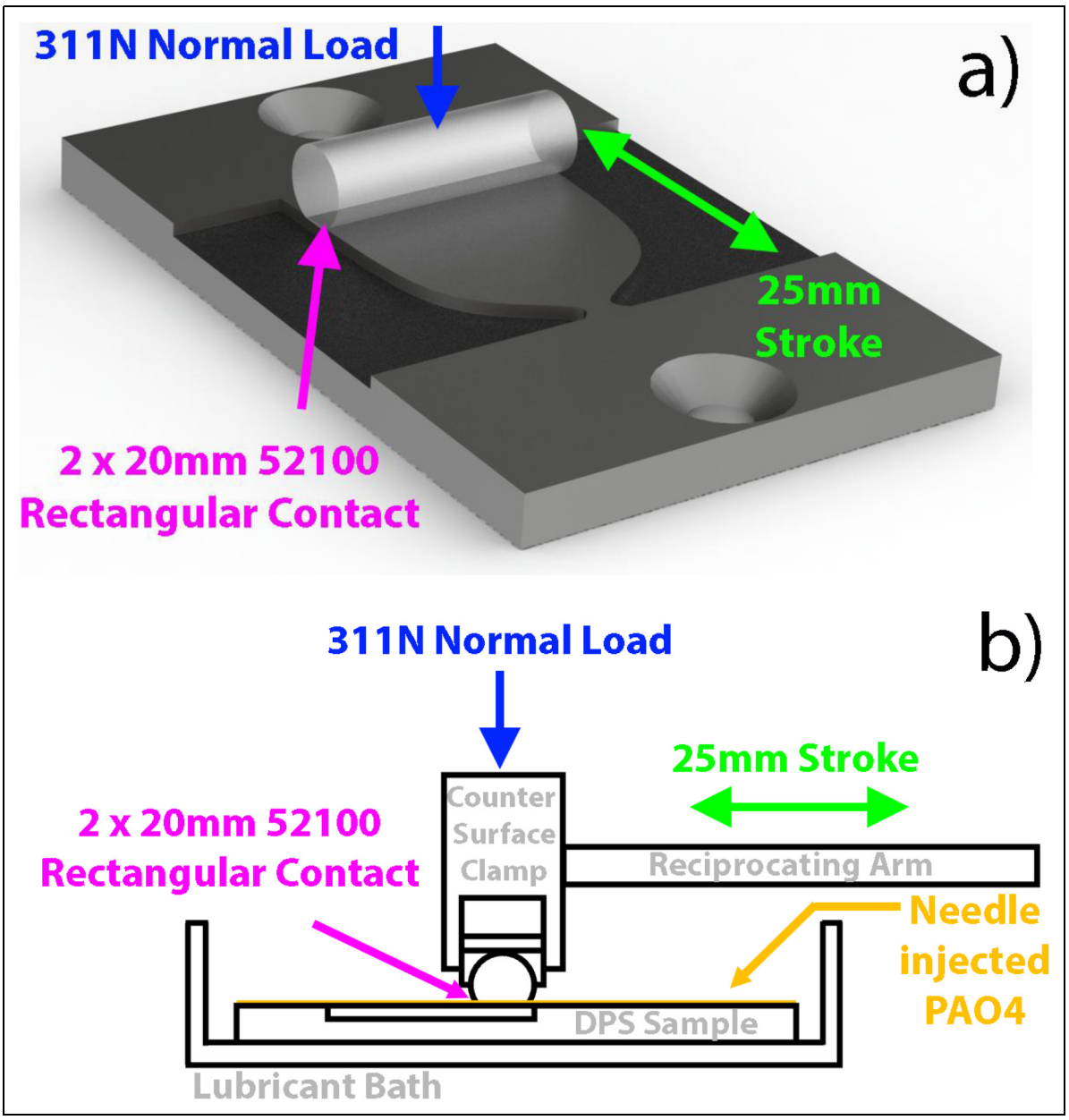

Figure 1. Schematics of (a) the dynamic pressure specimen configuration and (b) a cross section of the TE77 high frequency tribometer.

performed on both low and high loss edges with interpretation provided through Gatan Digital Micrograph software.

Results and discussion

Dynamic pressure test specimen

The Grade 250 flake graphite microstructure exhibited graphite flakes of several hundred micron lengths consistent with form I, distribution C and size 3 according to BS EN ISO 945-1:2008,[26] Figure 2(a). Flake graphite morphologies of this form and distribution have been shown to offer superior tribological performance compared to spheroidal classifications, delaying the onset scuffing because of the way the graphite is distributed during the early stages of sliding wear.[20,21,27,28] The dynamic pressure test surface can be seen in Figure 2(b) after the scuffing test. The rectangular counter surface exerting a nominal contact pressure of 7.9 MPa on the left part of the coupon, rising to 61.7 MPa at the high-pressure constriction on the right.

Friction behaviour

Upon commencement of sliding, there was an initial peak in the friction coefficient and contact potential at 5 N normal load, Figure 3(a)), which subsided as the normal load ramped to 311 N over a period of 300 s. Once the test load had been attained, the contact entered the mixed-to-boundary lubrication regime,[29–32] with an associated friction coefficient of 0.1 and contact potential values above 30 mV. As the temperature ramp continued

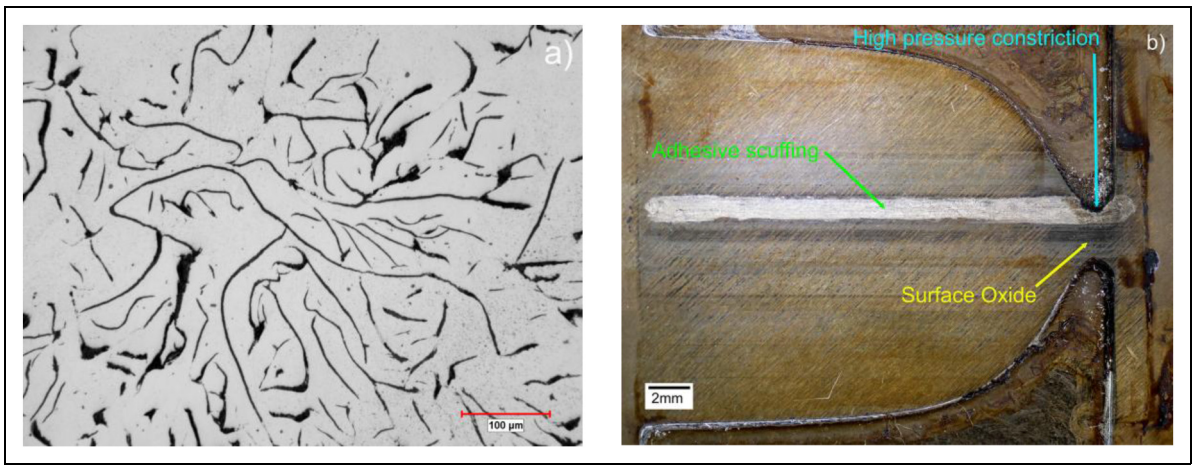

Figure 2. (a) Optical micrograph of Grade 250 flake graphite cast iron and (b) Digital image of scuffed dynamic pressure specimen.

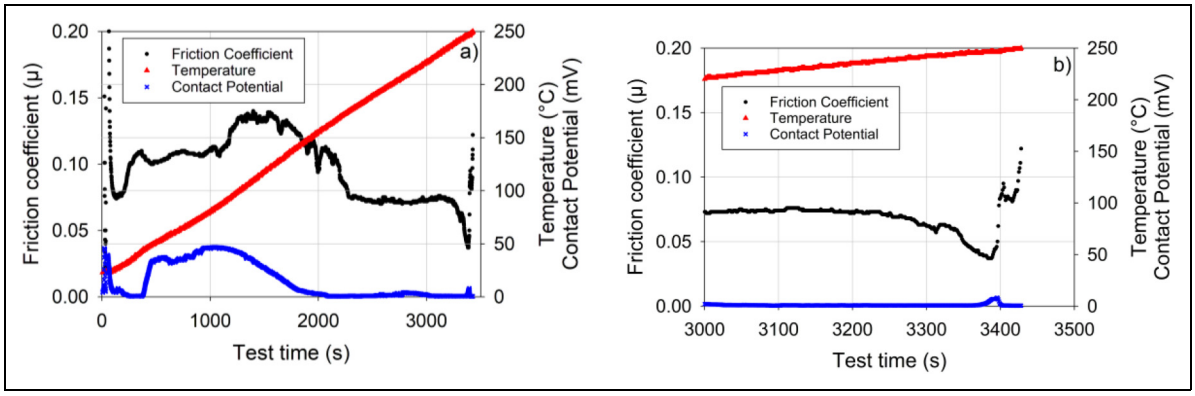

Figure 3. Friction coefficient, contact potential and specimen test temperature for (a) test duration and (b) end of test prior to scuffing.

past 75 °C, the friction coefficient began to rise towards 0.14. There was an associated decrease in the contact potential signal such that the contact had transitioned into the boundary lubrication regime by 2000 s sliding. Between 2000 and 3000 s, the friction coefficient was stable at 0.09 prior to decreasing at 3250 s to 0.04 whereupon scuffing initiated at 3370 s. Average coefficient of friction and standard deviation values just prior to scuffing are shown in Table 2.

Transitions in the contact potential signal over the duration of the test indicated three distinct regions, Figure 4. The transition from mixed lubrication to the boundary condition was the most obvious feature on the left of the image, prior to 2000 s. The stroke resolved contact potential signal also revealed a slight transitory increase between 2000 to 3000 s sliding time, especially near the high-pressure end of the contact. Prior to scuffing failure at 3370 s, there was a second transitory peak in the contact potential, commensurate with a notable decrease in the coefficient of friction to 0.04. Scuffing was identified by the rapid rise in friction coefficient and the onset of adhesive wear[20,21] which was clearly observed in Figure 3(b). These transitory changes in contact potential signal prior to scuffing suggested surface tribo-film formation under boundary lubrication conditions.

Raman

Raman spectroscopy from the highest contact pressure region indicated the presence of two surface oxide species, hematite (Fe_2O_3) and magnetite (Fe_3O_4), Figure 5(a). Mapping of the area shown in Figure 5(b) indicated that both oxides appeared mixed, with the magnetite phase appearing to be located at the surface of the contact. This could suggest a transformational oxidative wear mechanism based on the local asperity flash temperature that induces a phase transformation from hematite to magnetite prior to scuffing failure. This was similar to the findings of Yin et al.[33] who observed the formation of both hematite and magnetite phases when sliding martensitic and carbon steels against a WC ball.

Sub-surface analysis

A region from the high-pressure contact was selected for sub-surface investigations and lifted out for STEM EDX/EELS using the FIB/SEM, shown in the secondary electron image in Figure 6. This region was selected as it appeared to be raised from the surrounding surface, causing it to be the contacting area for the counter surface asperities as it

Table 2. Average friction coefficient and standard deviation values prior to scuffing.

	Boundary sliding	Pre-scuffing	Scuffing initiation
Test Time Interval (s)	3000–3300	3300–3400	3400–3428
Average Friction Coefficient	0.072 ± 0.003	0.052 ± 0.010	0.090 ± 0.010

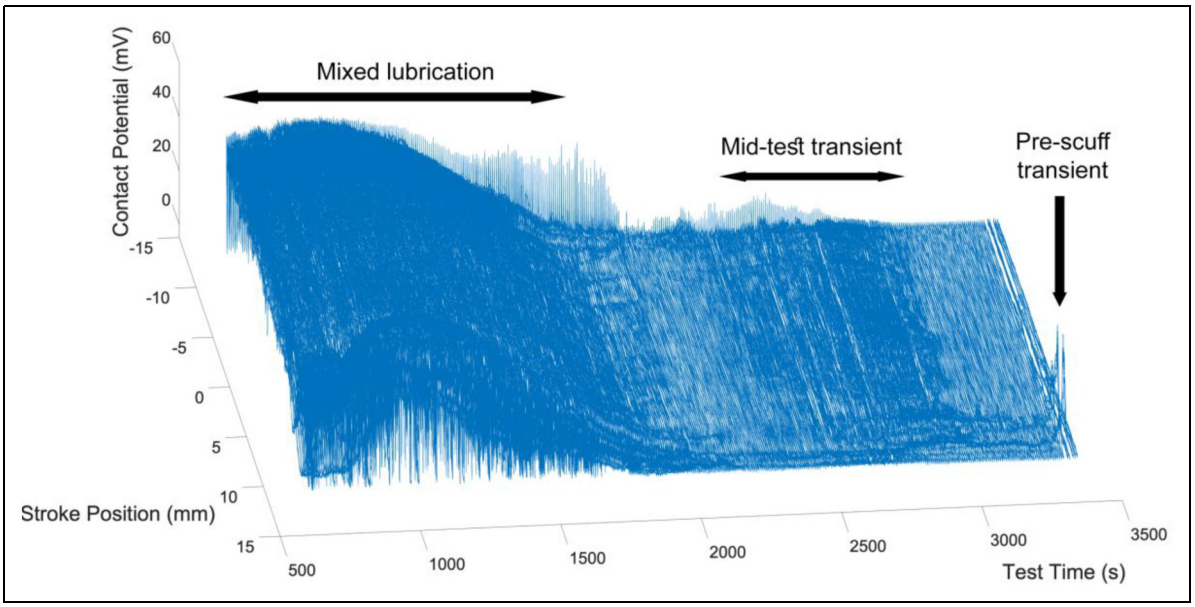

Figure 4. Contact potential signal as a function of stroke length and test time.

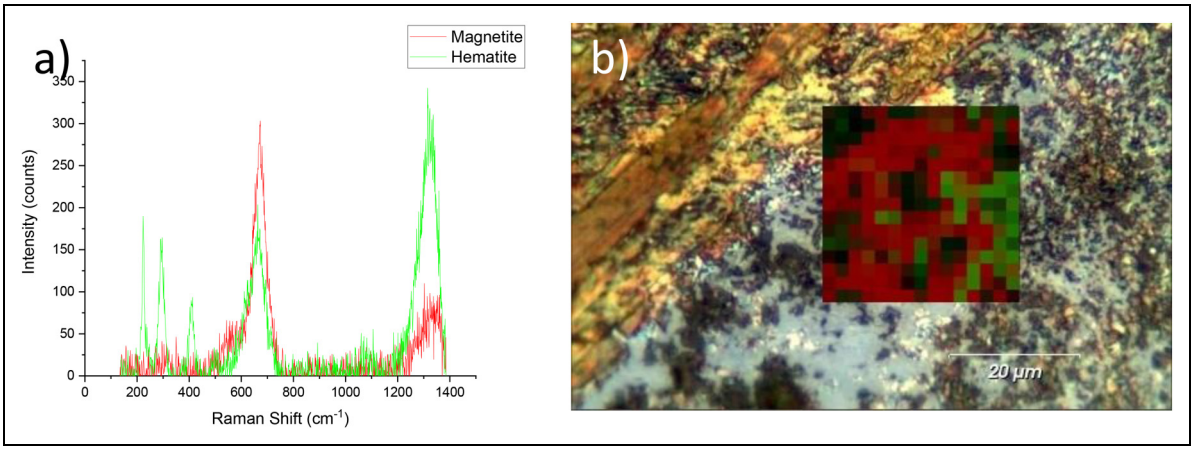

Figure 5. (a) Example Raman spectra for the two phases identified in the map and (b) corresponding map from high pressure surface where red is magnetite and green is hematite

traversed. The upper surface topography appeared to consist of fine nanoscale pores, giving the appearance of a porous surface and which were also present in other areas of the high contact pressure zone. It was interesting to note that there appeared a residual darker contrast substance underneath this feature as well as in surrounding pockets of tribological damage.

The HAADF image of the cross section shown in Figure 7(a) showed the upper Pt layer deposited to protect the surface, some of which was removed during final thinning to electron transparency on the right of the image. A HAADF image contains information of the material composition as the contrast shown is a factor of approximately Z^2. A layer with dark contrast separated the upper features from the bulk, which appeared to be composed to two distinct overlapping regions. This could be third body wear debris, which the high pressure contact region had caused to re-adhere to the cast iron surface. The porous upper layer was distinct due to the lower contrast, implying a composition of lower atomic number material.

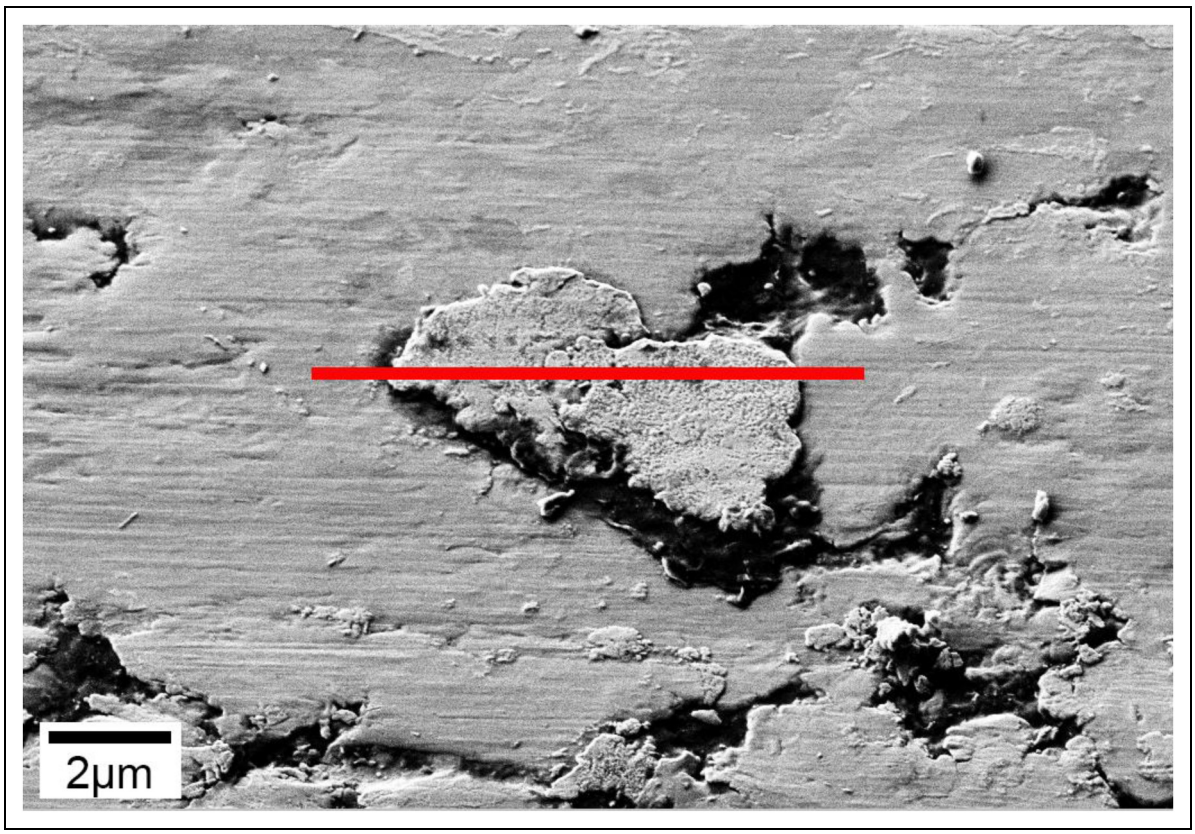

Figure 6. Secondary electron image from region of highest contact pressure (taken at 2 kV and 10° tilt).

The higher magnification bright field STEM image in Figure 7(b) strengthened the possibility that these surface features were wear debris particles, given the decrease in grain size compared to the bulk but also the distinct interlayer beneath their undersurface. STEM EDX mapping suggested a small amount of carbon present in addition to the iron signal, however the interlayer was chemically distinct by the observed distribution of mainly oxygen and silicon signals. As the polyalfaolefin molecular structure does not contain silicon, this points to a reaction from Si present in the composition of the Grade 250 cast iron, Table 1. This suggested that persistent elevated temperature sliding during the test was sufficient to oxidise elemental Si from the metallic surfaces to form polymeric Si-O siloxane species. This may have been responsible for a transitory increase in contact potential observed between 2000–3000 s sliding. This behaviour has been observed by Aiso et al.[34] in a carbon steel subject to cross cylinder sliding against TiN, where elevated flash temperatures initially caused SiO_2 to form, prior to the more complex oxide species containing Fe and other elements. They concluded that material transfer and friction behaviour was dominated by the most easily oxidised metal species present in the alloy composition. The influence of Si content on the machinability of steels has been noted to contribute to lower frictional cutting forces and tool wear due during high temperature (>1000 °C) machining due to transfer of oxidised Si based layers which protect the tool piece.[35,36] The steady decline in coefficient of friction values from 3250 s in the present work points to the onset of surface oxidation phenomena leading to a steady reduction in friction force prior to scuffing, Table 2. The siloxane phase appeared to be transitionary and mostly removed from the contact at the onset of scuffing. Evidence of it presence was only in recessed surface pockets and trapped between transferred wear debris. This represented a subtle transient in cumulative energy input scuffing testing methodologies that is absent from existing scuffing evolution models[17,23] where the kinetics of phase formation appear to play an important role.

A STEM EDX line scan was conducted through the upper nano-scale surface features, from bottom to top of the red line indicated in Figure 8(a). Carbon, gallium and platinum were all observed in the upper portion of the scan, attributed to the FIB deposited Pt layer to protect the nano-scale features from FIB beam artefacts. The bottom of the trace exhibited a strong iron signal as would be expected from a wear debris particle, but also a subtle oxygen signal. The iron signal decreased whilst the surface was approached however the oxygen signal exhibited a peak consistent with the nano-scale surface layer, suggesting that the frictional contact would be dominated by an oxidative surface species.

A higher magnification ADF STEM image of this surface layer, Figure 9(a), showed a nanoscale oxide surface film, similar to that observed by Saeidi et al.,[23] where nanocrystalline hematite (α-Fe_2O_3) and magnetite (Fe_3O_4) layers were observed on transferred wear debris

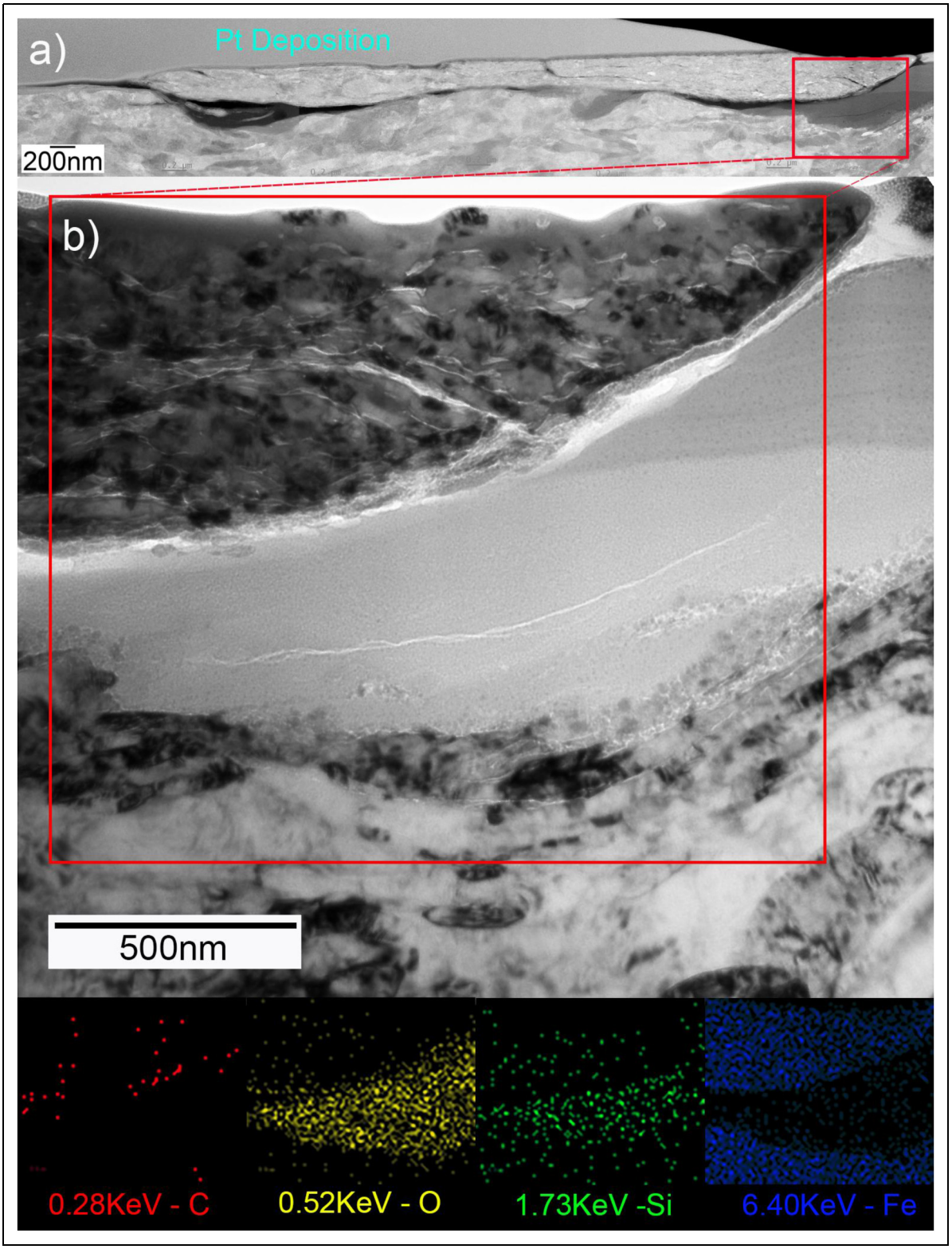

Figure 7. (a) Annular dark field STEM image of FIB section shown in Figure 6 and (b) corresponding bright field TEM image and STEM EDX maps for the region in red.

particles. In the present work significant comminution of the surface had led to a more elaborate evolution of surface species that facilitated the formation of a nanoscale surface oxide more consistent with a surface oxide 'glaze' layer. Such layers offer low friction between tribological material pairs through the oxidation and compaction of nano-scale surface species.[37–39] Electron energy loss spectroscopy from this region, Figure 9(b), indicated the presence of the Fe $L_{2,3}$ high-loss edges at 706 and 719 eV, consistent with the higher temperature Fe_3O_4[40] phase.

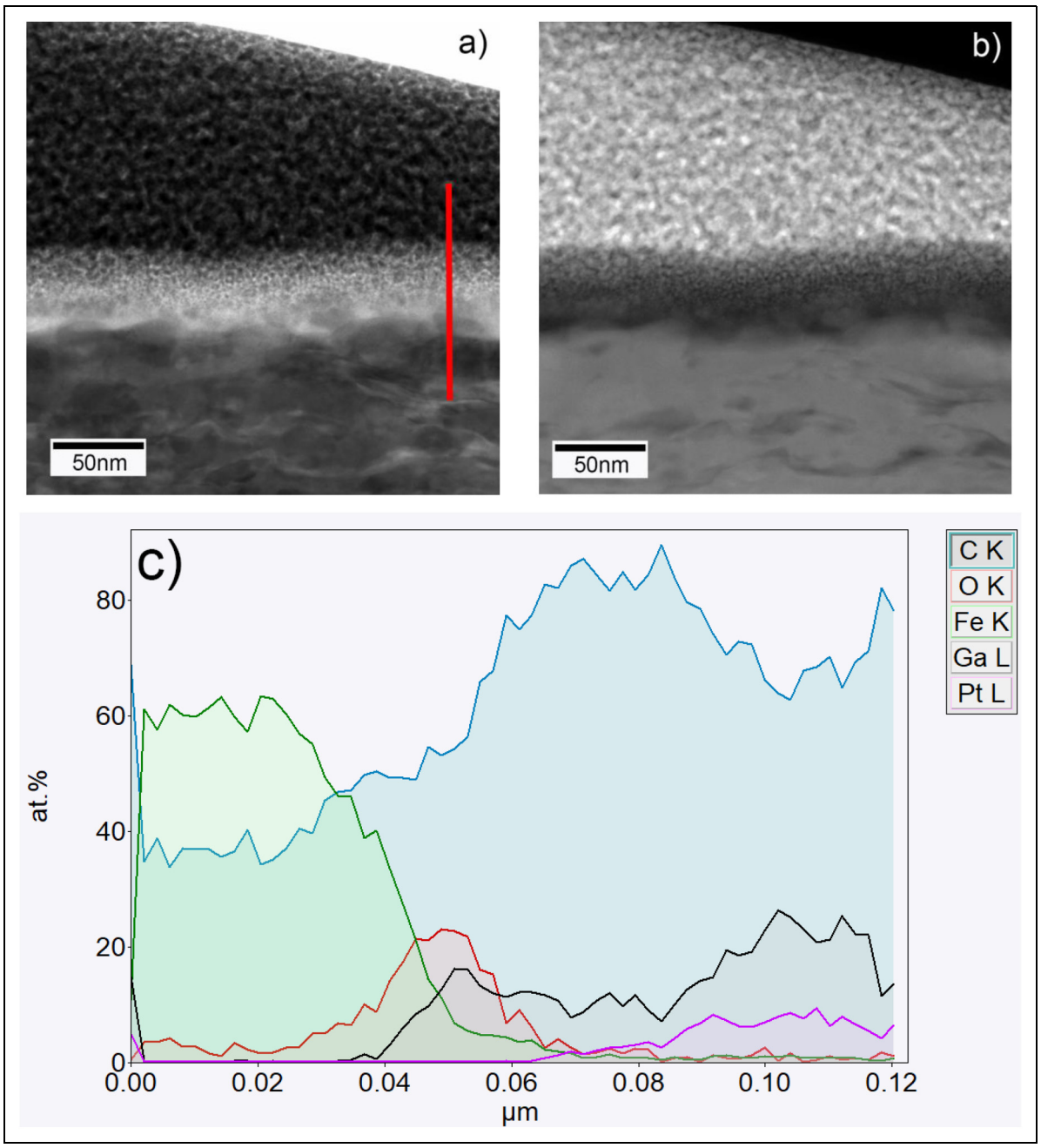

Figure 8. Bright field (a) and annular dark field (b) STEM images of the FIB section through the upper tribo-surface. The red line in (a) indicates the EDX line profile shown in (c).

Lattice fringe spacing from the particle indicated by the red line were measured to be 0.2158 ± 0.0142 nm, also consistent with a Fe_3O_4 magnetite phase.[41] Whilst similar hematite 'glaze' layers have been observed by Zhang et al.,[42] the upper layer appeared to be only composed of magnetite suggesting elevated flash temperatures from asperity contact.[33,43,44] Such layers are known to provide low friction behaviour in high temperature regimes where they can protect the sub-surface from direct frictional contact. Their absence may be why Saeidi et al.[23] did not observe a notable decrease in their average coefficient of friction prior to the onset of scuffing. The approach of starving a contact of lubricant to initiate scuffing often results in a shorter time to scuffing initiation. This can mitigate thermal energy accumulation, preventing the temperatures necessary for siloxane and oxide species formation and subsequent attrition and sintering.

The identification of transient siloxane formation indicated that the kinetic energy dissipation in the contact resulted in transient thermodynamic phase evolution. This ultimately culminated in a low friction surface oxide 'glaze' layer prior to the onset of scuffing failure. The formation of different thermodynamic transitional surface phases suggested frictional energy dissipation through abrasive asperity contacts locally increases the asperity contact temperature beyond the magnetite formation temperature,[33,44–46] consistent with Blok's critical temperature criteria.[47] This facilitating a mixed hematite and magnetite

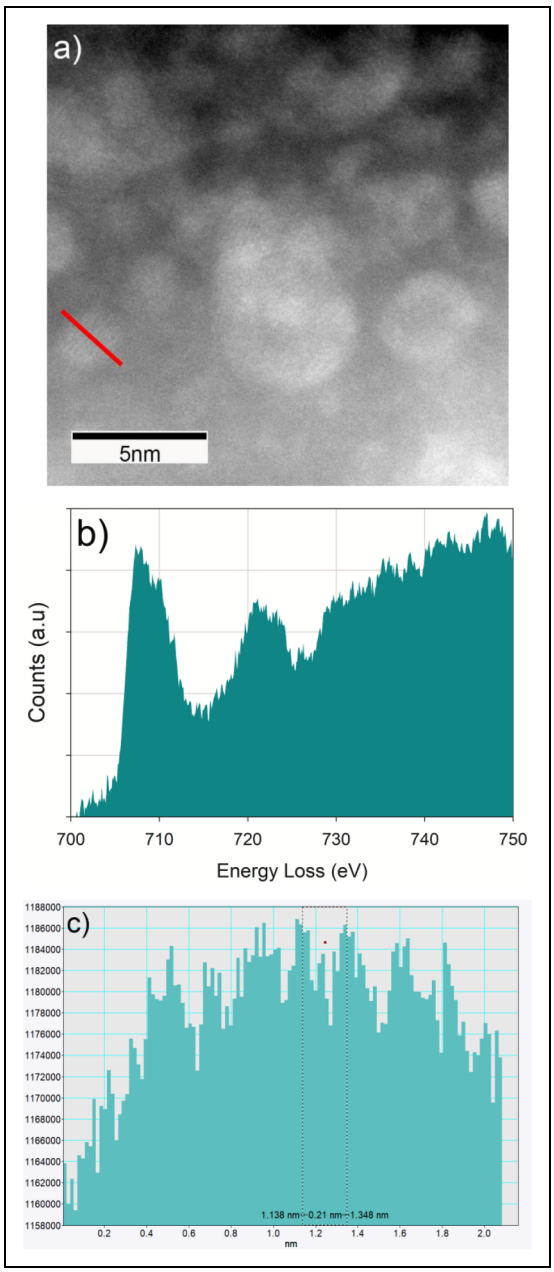

Figure 9. (a) Annular dark field STEM image of the surface from the high pressure contact region; (b) high-loss EELS spectrum and (c) lattice fringe spacing as indicated in (a).

oxide 'glaze' layer, with the latter phase dominating the surface frictional behaviour. Such mixed oxide tribolayers layers have been observed prior to scuffing[22,25,42] when the rate of transitions and energy input to the system (e.g., external heating, ramped load) facilitate formation rather than removal. In contrast rapid transients, sometimes observed with lubricant starvation,[23,48,49] can cause transitions and scuffing initiation to be more localised and rapid. Such oxide layers are conglomerates of third body particles with low interfacial cohesion.[50] They can exhibit plastic flow which facilitates the lowering of the coefficient of friction between first body surfaces whilst they are present.[33] Localised removal of the layer through asperity abrasion initiates cumulative degeneration and the onset of scuffing.[16,17,19,22,23] This is the ultimate step in a complex and interacting set of stages involving a multiplicity of chemical and thermodynamic surface reactions.

Conclusions

- A magnetite nano-crystalline surface oxide glaze layer formed on hematite was found to be responsible for low friction behaviour prior to failure in dynamic pressure scuffing of Grade 250 cast iron.
- FIB/STEM/EDX analysis revealed formation of transitory surface species such as siloxanes derived from the elemental composition of the flake graphite cast iron.
- Evidence of multi species formation indicated the transitory nature of thermodynamic phase formation in net energy input dynamic pressure sliding contacts.
- The resulting low friction behaviour contrasted to scuffing induced by lubricant starvation.
- Scuffing failure is the result of a complex interactive tribological system based on material and lubricant composition and the kinetics of phase formation induced by thermo-mechanical sliding.
- For engine applications utilising sustainable fuels, the presence of alternate chemical species in the fuel thus may impact the onset of scuffing initiation.

Acknowledgements

The authors acknowledge use of characterisation facilities within the David Cockayne Centre for Electron Microscopy, Department of Materials, University of Oxford, with the support of the Henry Royce Institute for advanced materials through the Researcher Access Scheme, funded from a grant provided by the Engineering and Physical Sciences Research Council (EP/X527257/1) and Mr Ahmed Sheita for the dynamic pressure testing and specimen manufacture.

Declaration of conflicting interests

The authors declared no potential conflicts of interest with respect to the research, authorship, and/or publication of this article.

Funding

The authors disclosed receipt of the following financial support for the research, authorship, and/or publication of this article: This work was supported by the Henry Royce Institute, (grant number EP/X527257/1).

ORCID iDs

John Walker https://orcid.org/0000-0003-2500-0077
Timothy Kamps https://orcid.org/0000-0002-6660-7070
Keith Paton https://orcid.org/0000-0003-0300-8676

References

1. Stępień Z. A comprehensive overview of hydrogen-fueled internal combustion engines: achievements and future challenges. *Energies* 2021; 14: 6504.
2. Onorati A, et al. *The role of hydrogen for future internal combustion engines*. London, England: Sage Publications Sage UK, 2022. pp.529–540.
3. Chiong M-C, et al. Advancements of combustion technologies in the ammonia-fuelled engines. *Energy Convers Manage* 2021; 244: 114460.
4. Nadimi E, et al. Effects of ammonia on combustion, emissions, and performance of the ammonia/diesel dual-fuel compression ignition engine. *J Energy Inst* 2023; 107: 101158.
5. Wouters C, et al. Comprehensive assessment of methanol as an alternative fuel for spark-ignition engines. *Fuel* 2023; 340: 127627.
6. Adril E, et al. Interaction effect and optimisation of temperature and residence time of co-pyrolysis for liquid fuel production. *Tribol Mater* 2025; 4: 165–176.
7. Dearnley PA. Meeting tribological challenges with surface engineered materials. *Tribol - Mater Surf Interf* 2007; 1: 18–27.
8. Cordtz RF, et al. An experimental study of the effect of condensing water vapour on the cold corrosion wear of marine engine cylinder liners. *Lubr Sci* 2022; 34: 103–111.
9. Doncoeur C, et al. Potential impacts of ammonia/hydrogen on engine lubricants: A review. *Front Energy* 2025; 19: 884–906.
10. Wang J, et al. A study on the tribological behavior of the piston ring-cylinder liner under ammonia conditions. *Wear* 2025; 584-585: 206427.
11. Lee PM and Chittenden RJ. Consideration of test parameters in reciprocating tribometers used to replicate ring-on-liner contact. *Tribol Lett* 2010; 39: 81–89.
12. Morina A, et al. Challenges of simulating 'fired engine' ring-liner oil additive/surface interactions in ring-liner bench tribometer. *Tribol - Mater Surf Interf* 2011; 5: 25–33.
13. Devo T, et al. Study of the wear process in an experimental simulation of a fuselage/runway rubbing contact. *Tribol Mater* 2024; 3: 1–14.
14. El-Sherbiny M. Cylinder liner wear. In: Tribology of Reciprocating Engines: Proceedings of the 9th Leeds–Lyon Symposium on Tribology Held in Bondington Hall, the University of Leeds, England 7–10 September 1982, 2017. Elsevier.
15. Li W, et al. Effects of cast-iron surface texturing on the anti-scuffing performance under starved lubrication. *Materials (Basel)* 2019; 12: 1586.
16. Walker JC, Jones HG and Kamps TJ. Dynamic pressure scuffing initiation of a grade 250 flake graphite cast iron. *Wear* 2023; 523: 204864.
17. Walker JC, et al. Variable pressure scuffing of a flake graphite cast iron diesel cylinder liner. *Tribol Int* 2023; 179: 108155.
18. Walker JC and Atkins B. Boundary-Lubricated dynamic-pressure sliding wear behavior of Grade 250 cast iron. *Tribol Trans* 2025; 68: 1–8.
19. Enthoven J and Spikes HA. Infrared and visual study of the mechanisms of scuffing. *Tribol Trans* 1996; 39: 441–447.
20. Kamps T, et al. Reproducing automotive engine scuffing using a lubricated reciprocating contact. *Wear* 2015; 332: 1193–1199.
21. Kamps T, et al. Scuffing mechanisms of EN-GJS 400-15 spheroidal graphite cast iron against a 52100 bearing steel in a PAO lubricated reciprocating contact. *Wear* 2017; 376: 1542–1551.
22. Lyu B, et al. Scuffing failure analysis based on a multiphysics coupling model and experimental verification. *Friction* 2024; 12: 1214–1234.
23. Saeidi F, et al. Origin of scuffing in grey cast iron-steel tribosystem. *Mater Des* 2017; 116: 622–630.
24. Lyu B, et al. Piston ring and cylinder liner scuffing analysis in dual-fuel low-speed engines considering liner deformation and tribofilm evolution. *Int J Engine Res* 2024; 25: 1776–1798.
25. Markut T, et al. Emergence of coated piston ring scuffing behavior on an application-oriented tribological model test system. *Lubricants* 2024; 12: 218.
26. B.S. Institution. *Founding — Grey cast irons*. London: BSI, 2011.
27. Hase A. Visualization of the tribological behavior of graphite in cast iron by in situ observations of sliding interfaces. *Tribol Int* 2019; 138: 40–46.
28. Tsujikawa M, et al. Influence of graphite morphology on dry sliding wear of flake graphite cast irons. *Int J Cast Met Res* 2008; 21: 76–80.
29. Hamrock BJ, Schmid SR and Jacobson BO. *Fundamentals of fluid film lubrication*. Boca Raton: CRC press, 2004.
30. Vencl A, et al. Structural, mechanical and tribological characterization of Zn25Al alloys with Si and Sr addition. *Mater Des* 2014; 64: 381–392.
31. Vencl A, et al. Production, microstructure and tribological properties of Zn-Al/Ti metal-metal composites reinforced with alumina nanoparticles. *Int J Metalcast* 2021; 15: 1402–1411.
32. Priest M. Factors influencing boundary friction and wear of piston rings. In: Dowson D, et al. (ed.) *Tribology series*. Leeds: Elsevier, 2000, pp.409–416.
33. Yin C-h, et al. Formation of a self-lubricating layer by oxidation and solid-state amorphization of nano-lamellar microstructures during dry sliding wear tests. *Acta Mater* 2019; 166: 208–220.
34. Aiso T, et al. Effect of combined additions of Si, Mn, Cr and Al to carbon steel on material transfer in a steel/TiN coated tool sliding contact. *Wear* 2017; 388: 9–17.
35. Aiso T and Matsumura T. Effect of si and al additions to steel on machinability in gear cutting. *ISIJ Int* 2022; 62: 1957–1966.
36. Umino M, et al. Effect of silicon content and lubricant on the machinability of hot working tool steel. *Tetsu-to-Hagane (In Japanese)* 2003; 89: 601–608.
37. Dreano A, et al. Influence of a pre-existing glaze layer on the fretting-wear response of HS25 cobalt-based alloy subjected to various temperature conditions. *Wear* 2022; 488: 204144.
38. Huang H, et al. Influences of counterparts on the high-temperature tribological properties and glaze layer formation of pre-oxidized cobalt-based alloys. *Wear* 2024; 544: 205260.
39. Mayer AR, et al. Recreating cobalt–based glaze layers through thermal spraying for extreme environments. *Wear* 2025; 570: 205972.
40. Colliex C, Manoubi T and Ortiz C. Electron-energy-loss-spectroscopy near-edge fine structures in the iron-oxygen system. *Phys Rev B* 1991; 44: 11402.
41. Golla-Schindler U, et al. Determination of the oxidation state for iron oxide minerals by energy-filtering TEM. *Micron* 2006; 37: 473–477.
42. Zhang B, et al. Evolution mechanism of wear characteristics of cylinder liner and piston ring under starved lubrication condition. *Tribol Int* 2025; 208: 110622.

43. Zhang B, et al. Reciprocating sliding friction behavior and wear state transition mechanism of cylinder liner and piston ring. *Wear* 2024; 546–547: 205293.
44. Quinn TFJ, Sullivan JL and Rowson DM. Origins and development of oxidational wear at low ambient temperatures. *Wear* 1984; 94: 175–191.
45. Baud J, Ferrier A and Manenc J. Study of magnetite film formation at metal-scale interface during cooling of steel products. *Oxid Met* 1978; 12: 331–342.
46. Yu X, et al. Tribological properties of magnetite precipitate from oxide scale in hot-rolled microalloyed steel. *Wear* 2013; 302: 1286–1294.
47. Blok H. *The postulate about the constancy of scoring temperature*, vol. 237. NASA Special Publication, 1970, p.153
48. Liu G-S, Li C-D and Liu S-J. Scuffing resistance property of Al-Si alloy cylinder liner after mechanical honing shaping under starved lubrication. *Australian J Mech Eng* 2025; 23: 1–13.
49. Wang Y, et al. Tribological properties of several surface-modified piston rings under extreme conditions. *J Tribol* 2024; 146: 011701.
50. Bouillanne O, et al. Wear in progress: how third body flow controls surface damage. *Tribol Lett* 2024; 72: 84.